

Submitted for publication to the Proceedings of the V International Conference on 'Applications of Physics in Medicine and Biology', Trieste, Italy, Sept. 2-6, 1996.

The Tomography Beamline at the National Synchrotron Light Source

F.A. Dilmanian¹, X.Y. Wu¹, E.C. Parsons¹, Jr., B. Ren¹, T.M. Button², L.D. Chapman³, X. Huang¹, S. Marcovici⁴, R. Menk⁵, M.J. Petersen⁶, C.T. Roque², W.C. Thomlinson⁵, Z. Zhong⁵

¹ Medical Department, Brookhaven National Laboratory, Upton, NY 11973-5000 (USA)

² Department of Radiology, School of Medicine, State University of New York, Stony Brook, NY 11794-8460 (USA)

³ Center for Synchrotron Research and Instrumentation, Illinois Institute of Technology, Chicago, IL 60616 (USA)

⁴ Analogic Corp., Peabody, MA 01960 (USA)

⁵ National Synchrotron Light Source, Brookhaven National Laboratory, Upton, NY 11973-5000 (USA)

⁶ Department of Surgery, School of Medicine, State University of New York, Stony Brook, NY 11794-8460 (USA)

RECEIVED

NOV 21 1996

OSTI

Abstract

MASTER

We compared the image contrast of a monochromatic CT, Multiple Energy Computed Tomography (MECT), being developed at the National Synchrotron Light Source for imaging the human head and neck, and a conventional CT scanner using phantoms. The same phantom images were also produced by computer simulations. The experimental results indicate that monochromatic CT, with a beam energy tuned just above the iodine K-edge, has \approx 3-fold advantage in iodine image contrast over conventional CT with a 120 kVp beam. Modeling the same polychromatic beam and a monochromatic beam of the same mean energy at the same 3-rad dose and 3-mm slice height on an 18-cm-diameter acrylic phantom, the simulations show a noise of 1.2 HU for MECT and 1.9 HU for CCT. Furthermore, despite the Cupping-effect corrections the bone contrast is lower in CCT and varies by 24 HU moving from the phantom's center to the edge; this indicates an advantage for MECT in detecting and quantifying lesions differing from surrounding tissue by their effective mean atomic number.

DISTRIBUTION OF THIS DOCUMENT IS UNLIMITED

UM

DISCLAIMER

This report was prepared as an account of work sponsored by an agency of the United States Government. Neither the United States Government nor any agency thereof, nor any of their employees, makes any warranty, express or implied, or assumes any legal liability or responsibility for the accuracy, completeness, or usefulness of any information, apparatus, product, or process disclosed, or represents that its use would not infringe privately owned rights. Reference herein to any specific commercial product, process, or service by trade name, trademark, manufacturer, or otherwise does not necessarily constitute or imply its endorsement, recommendation, or favoring by the United States Government or any agency thereof. The views and opinions of authors expressed herein do not necessarily state or reflect those of the United States Government or any agency thereof.

DISCLAIMER

**Portions of this document may be illegible
in electronic image products. Images are
produced from the best available original
document.**

1. Introduction

The new generation of synchrotron x-ray beamlines have allowed the use of monochromatic x rays in medical imaging in general, and in computed tomography (CT) in particular. Monochromatic CT studies have been carried out at Stanford Synchrotron Radiation Laboratory (SSRL) [1], at the National Synchrotron Light Source (NSLS) [2-5], and at the Photon Factory, Tsukuba, Japan [6]. The rationale for this extensive work is that monochromatic CT has several basic advantages beyond those of conventional CT (CCT). In particular, monochromatic beams a) eliminate beam hardening artifacts; b) allow CT at optimal beam energy for a given subject size [8,9]; and c) allow energy-selective imaging, such as contrast CT above the K-edge of the contrast element and dual-energy quantitative CT (DEQCT) [10], which is the application of dual photon absorptiometry [11] in the CT mode. This paper describes the state of the CT beamline at the NSLS and presents our new results on image contrast. The program, Multiple Energy Computed Tomography (MECT), uses the Synchrotron Medical Research Facility (SMERF) which, since its establishment has been hosting the Transvenous Coronary Angiography program. MECT uses a fixed horizontal fan-shaped beam and a subject apparatus rotating about a vertical axis. This paper reports our measurements of image contrast measurements with and without the use of contrast agents.

1.1. Image contrast-to-noise ratio

The image characteristics most relevant to the system's ability to differentiate a lesion from its background is the contrast-to-noise ratio (CNR), which is defined for a given subject's contrast. Therefore, to compare two different CT systems their image contrasts and their image noises should be measured. Image contrast is related to the attenuation coefficient of the subject and therefore depends only on the beam's energy spectrum and can be compared easily between the two systems. On the other hand, image noise cannot be easily compared because it depends on the system's spatial resolution. Quantitatively, the variance σ^2 of the CT number in image of a uniform subject, for a given dose, is inversely proportional to the slice thickness and the square of the in-plane spatial resolution. The latter is a function of several parameters in the system and in the image reconstruction routine, including the focal-spot size, detector's resolution, the imaging and the reconstruction geometries, the pixel size, and the reconstruction filter. Since all these parameters differ between MECT and CCT, matching the images' noise in the two systems by any compensatory arrangement is virtually impossible. For this reason, we used computer simulations to compare the image noise in MECT and CCT, while we carried out experiments and simulations to evaluate image contrast in I- and Gd-filled phantoms. The effect of beam hardening on bone's image contrast only was simulated.

1.2. Image contrast using a contrast agent

The advantage of a narrow-energy-band beam in contrast imaging is that the beam energy can be tuned just above the K-edge of the contrast element, thus maximizing image contrast. Fig. 1 demonstrates this effect by superimposing the x-ray attenuation coefficient in iodine as a function of the photon energy, on the energy spectrum of a 120-kVp beam filtered with a 0.125 mm Cu foil.

We note, however, that the above-the-edge beam energy for iodine, ≈ 33.3 keV, is not optimized for imaging the human body except, probably, for the neck or limbs. For this reason, the future prospects for development of a compact, clinical narrow-energy-band CT may entail development of CT contrast agents based on heavier-than-iodine elements such as Gd (K-edge of 50.23 keV). Fig. 2 shows a plot similar to that of Fig. 1, except the Gd

attenuation curve is used instead of that for iodine.

1.3. Image contrast and quantification in tissue

In general, tissue can be characterized for CT imaging in terms of two parameters: its electron density, and its effective mean atomic number. To fully characterize a tissue in this way dual-photon absorptiometry in the CT mode is needed [12] (for which a monochromatic beam is highly advantageous). For a single measurement, however, the effective mean atomic number is most often the dominating factor. This is the reason why soft-tissue contrast is almost eliminated when very high kVp values are used because the Z-effect diminishes at high energies. This effect is shown best by comparing the attenuation curves of bone and soft tissue (Fig. 3). Depending on the beam's energy spectrum, the effective atomic numbers of these two tissue-types are about 16 and about 10, respectively. In characterizing soft-tissue, however, the limit of lesion detectability for a CT system can be a small fraction of one atomic number, depending on the image noise and on the beam's effective energy. As shown in Fig. 3 (which is plotted on a linear ordinate to emphasize the slopes of the curves), a small reduction in beam energy leads to a steeper region on the two curves where the difference in the attenuation coefficients of bone and soft tissue are enhanced. The findings discussed below show that by using a monochromatic CT a lower effective beam energy can be employed (for the same subject dose), resulting in a gain in the Z-dependent component of the tissue's image contrast. Furthermore, because the effective beam energy in monochromatic CT stays close to the incident beam energy throughout the image, quantification of the tissue's attenuation coefficient is much more precise in the monochromatic CT.

2. Experimental Design

2.1. The MECT system

The NSLS X-ray storage ring (energy: 2.5 GeV; maximum ring current: 300 mA) operates 29 beamlines with 2-3 beamports at each beamline [13]. MECT uses the X17B2 superconducting wiggler beamline. The state of the MECT system used during the present studies is described in Refs. 4-6. In particular, the monochromator was a tunable, two-crystal Laue-Laue, fixed-exit device employing flat Si <111> crystals with an energy range of 24-52 keV [14]. The detector was a linear-array modular CdWO₄-photodiode device with a 1.844-mm element spacing [15] masked to a 0.922-mm active element width element to improve the spatial resolution. The data acquisition system (DAS) included a current-filtering front-end unit developed by Analogic Corp., connected to a DEC Alpha computer through a custom-designed interface. It provided a usable signal dynamic range of \approx 500,000:1.

The source-subject and the subject-detector distances were 39 m and 2 m, respectively. The size of the source spot was 0.95 mm and 0.05 mm FWHM in the horizontal and vertical directions, respectively.

2.2. The CCT system

The CCT used was a GE HiSpeed CT scanner [16] at the Department of Radiology, Health Sciences Center, State University of New York, Stony Brook. The system's energy spectra at 80, 100, and 120 kVp were estimated on the basis of the beams' measured half-value layers (HVLs). The information was used then to calculate beam's filtration at these individual kVp settings. Table 1 summarizes the results.

2.3. Data collection parameters

The rate at which projections were collected was 1440/s, while the subject apparatus rotated at the rate of 24°/s. During the off-line image analysis, 24 such projections were averaged to form one projection for reconstruction. Reference data (i.e., data taken with no subject in the beam) collected before and after each subject slice were scanned. Two separate 360° data were collected with one lateral translation of the subject's rotation axis corresponding to one-half of one inter-element detector spacing between collections, and were interlaced during the reconstructions [3,5]. Short-term oscillations of the beam's intensity were compensated by using data from the two unattenuated ends of the fan beam, designated "air channels". Linear variations of the beam profile's shape were corrected by linear interpolation between these ends.

3. Computer Simulations

The program did not follow individual photons but used synthetic normal noise to broaden the counts in each ray, which were traced from the source to individual detector elements, and for each single energy value. Detector and DAS noise were assumed to be negligible. For the polychromatic beam, 1-keV energy steps were used. The detector signal was set as the counts times the beam energy (i.e. assuming a perfect detector sensitivity). The same image reconstruction routine used for experimental data was applied to the results. All the phantoms simulated were cylindrical ones and were imaged axially. First-order beam hardening effects (Cupping effect) were corrected for in the polychromatic images. The simulations presented below differ from the experiments by one detail, they employ a 0.922 mm-pitch detector (with 0.25 mm inactive band) instead of using a 1.844 mm-pitch detector masked to 0.922 mm used in the experiments. The same effective detector resolution was used for MECT and CCT.

4. Results from experiments and simulations

Two different acrylic phantoms were used, one with a 13.5 cm diameter and the other one with 18 cm. Each included thirty 11-mm diameter paraxial channels filled with different sets of diluted solutions of different contrast agents. Fig. 4 shows the pattern of the channels and their contents for the 18-cm phantom; Table 2 lists the concentrations of iodine and gadolinium in different channels. The Gd agent was Magnevist [17], a brand of gadopentetate dimeglumine with a chemical composition of $C_{28}H_{54}GdN_5O_{20}$. The individual measurements are described below.

4.1. Gadolinium image contrast - MECT vs. CCT

The 18-cm phantom was imaged with MECT at above and below the Gd K-edge, 50.34 and 50.10 keV. Fig. 5 shows the above- (top) and below-edge (middle) images, as well as the subtracted image (bottom). The phantom was also imaged with CCT at 120 kVp (not shown). The experimental MECT images were obtained at 2 rad surface dose and 3 mm slice height, using a Hanning filter at a 0.6 cutoff frequency; the image noises in the two direct images were 2 HU.

Table 3 summarizes image contrast and noise obtained with MECT and CCT experimentally or by simulations for the 1600 μg Gd/ml-channel in the phantom described above. It also includes simulated CNR. MECT's experimental results are given only for above Gd's K-edge, while MECT's simulations also included 60.5 keV, which was the mean

spectral energy of the CCT's 120 kVp beam. Simulations for both MECT and CCT were made at 3 rad surface dose and 3-mm slice height, using a Hanning filter at a 0.6 cutoff frequency.

We note that in Fig. 5 that five sequential Gd channels in one set (the horizontal one, going from left to right for decreasing concentrations) can be differentially visualized from each other. This means that the image sensitivity is $\approx 100 \mu\text{g Gd/cc}$. Scaling the CNR of 76 obtained for $1600 \mu\text{g Gd/ml}$ to $100 \mu\text{g Gd/ml}$, we find that the minimal observable concentration corresponds to a CNR of 4.8, which is compatible with Rose's condition [18] that set the detectable CNR to 5.

We also note from Table 3 that the MECT/CCT ratio of CNR is 2.8:1.0 for 50.3 keV MECT and 2.3:1.0 for 60.5 keV MECT.

4.2. Iodine image contrast - MECT vs. CCT

The 13.5 cm phantom with iodine concentrations ranging from 240 to $0 \mu\text{g I/ml}$ was used for these experiments and simulations. MECT's images were obtained at above the iodine K-edge, 33.25 keV, and at 43 keV; CCT images were taken at 80 and 100 kVp. Table 4 summarizes our results for image contrast for the $240 \mu\text{g I/ml}$ channel in the phantom, and for image noise. The table includes also data on CCT's experimental image contrast for 120 kVp, 8 HU, which was scaled from the 42 HU result obtained with the $1200\text{-}\mu\text{g I/ml}$ channel of the 18-cm phantom.

We note that the ratio of the image contrast in MECT (at 33.25 keV) to that in CCT (at 120 kVp) is 3.1:1.0.

4.3. Tissue contrast - MECT vs. CCT

As indicated in Table 3, the simulated noises in the 18-cm phantom were the same for the 60.5-KeV-MECT and the 120-kVp-CCT images obtained at equal surface doses. However, the *effective* mean spectral energy of the beams throughout the phantom in these two images is not the same because the 120-kVp beam hardens in traversing the subject. To quantify this effect simulations were carried out using an 18-cm diameter cylindrical water phantom with two cylindrical, 6-mm diameter, paraxial bone inserts, one at the phantom's center and one positioned at the edge, 7 cm from the phantom's center. The image contrast for each bone was simulated with 120-kVp CCT and 60.5-keV MECT (i.e. the same mean spectral energy). The results, summarized in Table 5, indicate the following residual beam-hardening effects. First, the bone contrast obtained with CCT is lower than that expected from the incident beam in average by 100 HU; this corresponds to a beam hardening of 2.75 keV. Second, the bone contrast decreases by ≈ 20 HU going from the edge of the phantom to its center, which corresponds to a differential beam hardening of 0.5 keV.

5. Summary and Discussion

MECT's image noise in all images presented is lower than that of CCT. Furthermore, regarding imaging with contrast agents We reached the following conclusions. First, with the monochromatic beam tuned just above the K-edge of the contrast element, MECT has a significant advantage in image CNR compared to CCT. The quantitative advantage in image contrast in our particular geometry, with CCT operating at 120 kVp, was 3.1:1.0 for iodine and 2.1:1.0 for gadolinium. Second, for the same volume of contrast agent reaching the target organ, Gd has a larger image contrast than iodine when both are

imaged with CCT at 120 kVp. This judgement comes from the fact that the CCT's measured image contrast at 120 kVp for the phantom's 1600 μg Gd/ml-channel was 64 HU for CCT, while that for 1200 μg I/ml was 42 HU (which relates to 56 HU for 1600 μg I/ml), i.e. an advantage of $\approx 1.16:1.00$ for Gd. On the other hand, Gd with monochromatic CT has an 2.5:1.0 advantage in image contrast over iodine with CCT (138 and 56 HU, respectively for imaging 1600 μg Gd/ml).

The advantages of MEECT in tissue imaging with no contrast agent come about in two ways. First, the effective beam energy of MEECT for the same subject dose and image noise is smaller than CCT, causing a larger differentiation between two tissues differing from each other in their effective mean atomic numbers. Second, MEECT's constant and known effective beam energy throughout the image makes it a highly quantitative system.

MEECT's first clinical studies will be dual-energy quantitative CT (i.e. dual photon absorptiometry) for imaging the composition of carotid artery plaques, and CT angiography using iodine or gadolinium contrast agents.

Acknowledgements

We thank J.A. Coderre, J.M. Dobbs, F. Giron, N.F. Gmür, D. Greenberg, J.B. Hastings, D.D. Joel, J. Kress, Z. Liang, M.H. Miller, M.M. Nawrocky, M. Shleifer, D.P. Siddons, D.N. Slatkin, A.D. Woodhead, and K. Yamamoto for assistance. This work was supported by the Office of Health and Environmental Research, U.S. Department of Energy.

REFERENCES

- [1] Thompson AC, Llacer J, Finman L C, Hughes EB, Otis JN, Wilson S, Zeman HD. Computed tomography using synchrotron radiation. Nucl Instr and Meth 1984: 222; 319-323.
- [2] Dilmanian FA, Garrett RF, Thomlinson WC, Berman LE, Chapman LD, Gmür NF, Lazarz NM, Luke PN, Moulin HR, Oversluisen T, Slatkin DN, Stojanoff V, Thompson AC, Volkow ND, Zeman HD. Multiple Energy Computed Tomography for neuroradiology with monochromatic x-rays from the National Synchrotron Light Source. Physica Medica 1990: 6; 301-307.
- [3] Dilmanian FA. Computed tomography with monochromatic x rays. Am. J. Physiol. Imaging 1992: 3/4; 175-193.
- [4] Wu XY, Dilmanian FA, Chen Z, Ren B, Slatkin DN, Chapman D, Shleifer M, Staicu FA, Thomlinson W. Multiple Energy Computed Tomography (MEECT) at the NSLS: Status report. Rev Sci Instrum 1995: 66; 1346-1347.
- [5] Dilmanian FA, Wu XY, Parsons EC, Ren B, Kress J, Button TM, Chapman LD, Coderre JA, Giron F, Greenberg D, Krus DJ, Liang Z, Marcovici S, Petersen MJ, Roque CT, Shleifer M, Slatkin DN, Thomlinson WC, Yamamoto K, Zhong Z. Single- and dual-energy CT with monochromatic synchrotron x rays. Accepted for publication in Phys Med Biol.
- [6] Takeda T, Itai Y, Hayashi K, Nagata Y, Yamaji H, Hyodo K. High Spatial Resolution CT with a synchrotron radiation system. J Comput Assist Tomogr 1994: 18; 98-101.
- [7] Grodzins L. Optimal energies for x-ray transmission tomography of small samples. Nucl Instr and Meth 1983: 206; 541-545.
- [8] Grodzins L. Critical absorption tomography of small samples. Nucl Instr and Meth

- 1983: 206; 547-552.
- [9] Spanne P. X-ray energy optimization in computed microtomography. *Phys Med Biol* 1989: 34; 679-690.
 - [10] Cann CE, Genant HK. Precise measurement of vertebral mineral content using computed tomography. *J Comp Assist Tomogr* 1980: 4; 493-500.
 - [11] Pepler WW, Mazess RB. Total body bone mineral and lean body mass by dual-photon absorptiometry. *Calcif Tissue Int* 1981: 33; 353-359.
 - [12] McCullough EC. Computed tomography in radiation therapy treatment planning. In: *Radiology of the skull and brain - Technical Aspects of Computed Tomography*. Vol. Five. Newton TH and Potts DG Eds. The C.V. Mosby Company, St. Louis 1981; 4301-4311.
 - [13] van Steenbergen A and NSLS Staff. The National Synchrotron Light Source, basic design and project status. *Nucl Instr and Meth* 1980: 172; 25-32.
 - [14] Shleifer M, Dilmanian FA, Staicu FA, Woodle MH. Mechanical design of a high-resolution tunable crystal monochromator for the Multiple Energy Computed Tomography project. *Nucl Instr and Meth* 1994: A 347; 356-359.
 - [15] On loan from Analogic Corporation, Peabody, MA 01960, USA.
 - [16] General Electric Medical Systems, Milwaukee, WI 53201, USA.
 - [17] Berlex Laboratories, Wayne, NJ 07470, USA.
 - [18] Rose A. The sensitivity performance of the human eye on an absolute scale. *J Opt Soc Am* 1948: 38; 196-208.

Table 1

| kVp setting | HVL, in mm of Al | Spectral mean energy (keV) | Estimated beam's filtration |
|-------------|------------------|----------------------------|-----------------------------|
| 80 | 4.23 | 42.8 | 2.5 mm Al |
| 100 | 5.75 | 55.1 | 2.5 mm Al + 0.125 mm Cu |
| 120 | 7.05 | 60.5 | 2.5 mm Al + 0.125 mm Cu |

Table 2
Concentration of I and Gd in the phantom's channels

| <u>Iodine Concentrations</u> | | <u>Gadolinium Concentrations</u> | |
|------------------------------|-----------------------|----------------------------------|-----------------------|
| 1: | 1200 $\mu\text{g/ml}$ | A: | 1600 $\mu\text{g/ml}$ |
| 2: | 850 $\mu\text{g/ml}$ | B: | 800 $\mu\text{g/ml}$ |
| 3: | 575 $\mu\text{g/ml}$ | C: | 400 $\mu\text{g/ml}$ |
| 4: | 350 $\mu\text{g/ml}$ | D: | 200 $\mu\text{g/ml}$ |
| 5: | 200 $\mu\text{g/ml}$ | E: | 100 $\mu\text{g/ml}$ |
| 6: | 100 $\mu\text{g/ml}$ | F: | 50 $\mu\text{g/ml}$ |
| 7: | 50 $\mu\text{g/ml}$ | G: | 25 $\mu\text{g/ml}$ |
| 8: | 0 $\mu\text{g/ml}$ | H: | 0 $\mu\text{g/ml}$ |

Table 3
Image Contrast for 1600 $\mu\text{g Gd/ml}$ and Image Noise

| System | Beam Energy | Experimental | | Simulated | | Simulated CNR |
|--------|-------------|---------------|------------|---------------|------------|---------------|
| | | Contrast (HU) | Noise (HU) | Contrast (HU) | Noise (HU) | |
| MECT | 50.34 keV | 138 | 2.0* | 137 | 1.4 | 98 |
| | 60.5 keV | - | - | 98 | 1.2 | 82 |
| CCT | 120 kVp | 64 | - | 66 | 1.9 | 35 |

* Different parameters from the simulations

Table 4
Image Contrast for 240 $\mu\text{g I/ml}$ and Image Noise

| System | Beam Energy | Experimental Contrast (HU) | Simulated Contrast (HU) | Simulated Noise (HU) | Simulated CNR |
|--------|-------------|----------------------------|-------------------------|----------------------|---------------|
| MECT | 33.25 keV | 26 | 26 | 1.3 | 20.0 |
| | 43.0 keV | 18 | 17 | 1.0 | 17.0 |
| CCT | 80 kVp | 13 | 12 | 1.3 | 9.2 |
| | 100 kVp | 9 | 9 | 1.2 | 7.5 |
| | 120 kVp | 8.4 | 8 | 0.9 | 8.9 |

Table 5
Bone Contrast simulated inside an 18-cm Water Phantom

| System | Contrast for incid. beam (HU) | On Phantom's center | | On Phantom's edge | |
|------------------|-------------------------------|---------------------|---------------------|-------------------|---------------------|
| | | Contrast (HU) | Effective En. (keV) | Contrast (HU) | Effective En. (keV) |
| MECT at 60.5 keV | 1431 | 1429 | 60.56 | 1433 | 60.46 |
| CCT at 120 kVp | Not defined* | 1304 | 63.52 | 1324 | 63.03 |

* The term is not meaningful as the contrast depends on the subject's size

Figure Captions

- Fig. 1. X-ray total attenuation coefficients in gadolinium superimposed on a 120-kVp beam energy spectrum.
- Fig. 2. X-ray total attenuation coefficients in iodine superimposed on a 120-kVp beam energy spectrum.
- Fig. 3. X-ray total attenuation coefficient is bone and soft tissue.
- Fig. 4. Pattern of channels filled with different Gd and I solutions in the 18-cm phantom (see Table 2).
- Fig. 5. MECT images of the 18-cm phantom: above the Gd edge (top), below the edge (center), and subtracted (bottom).

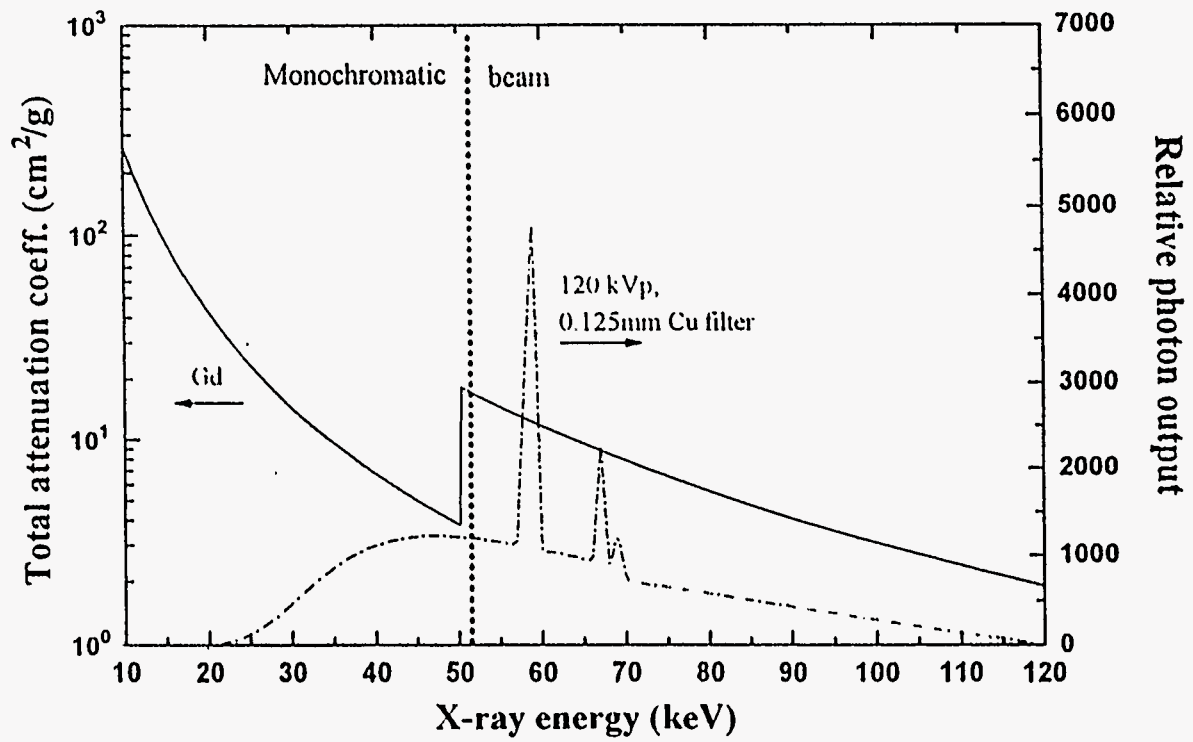


Figure 1

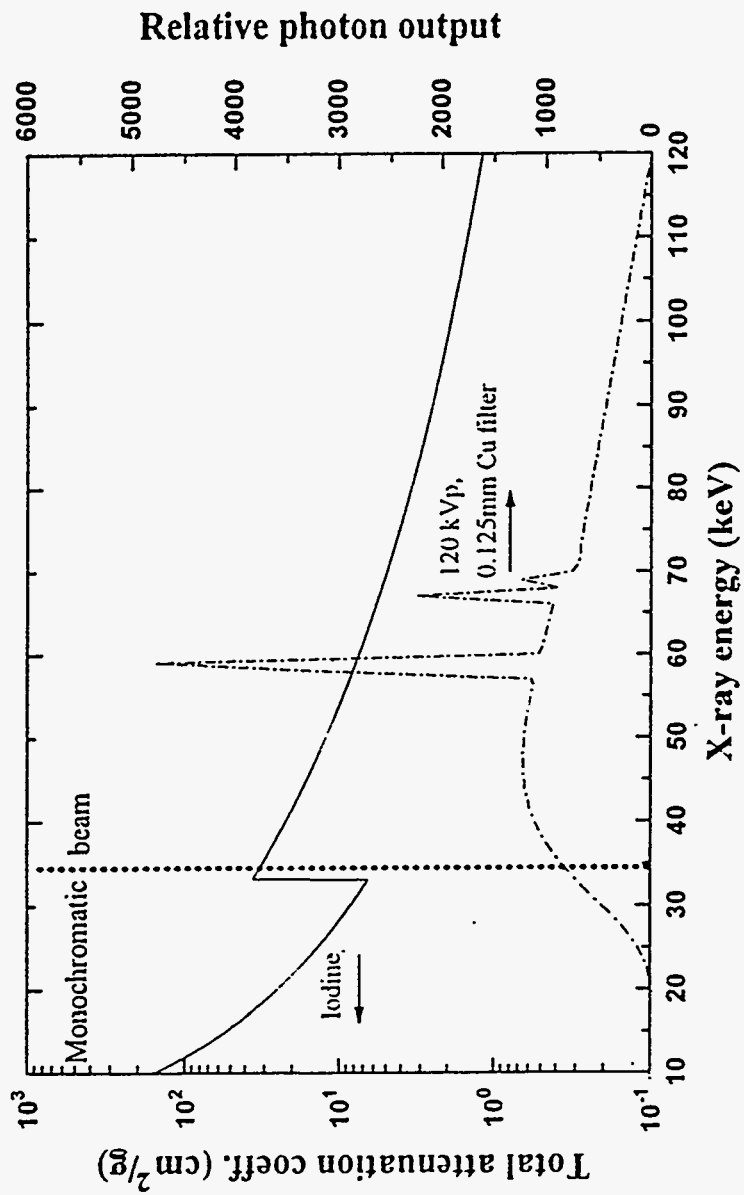


Figure 2

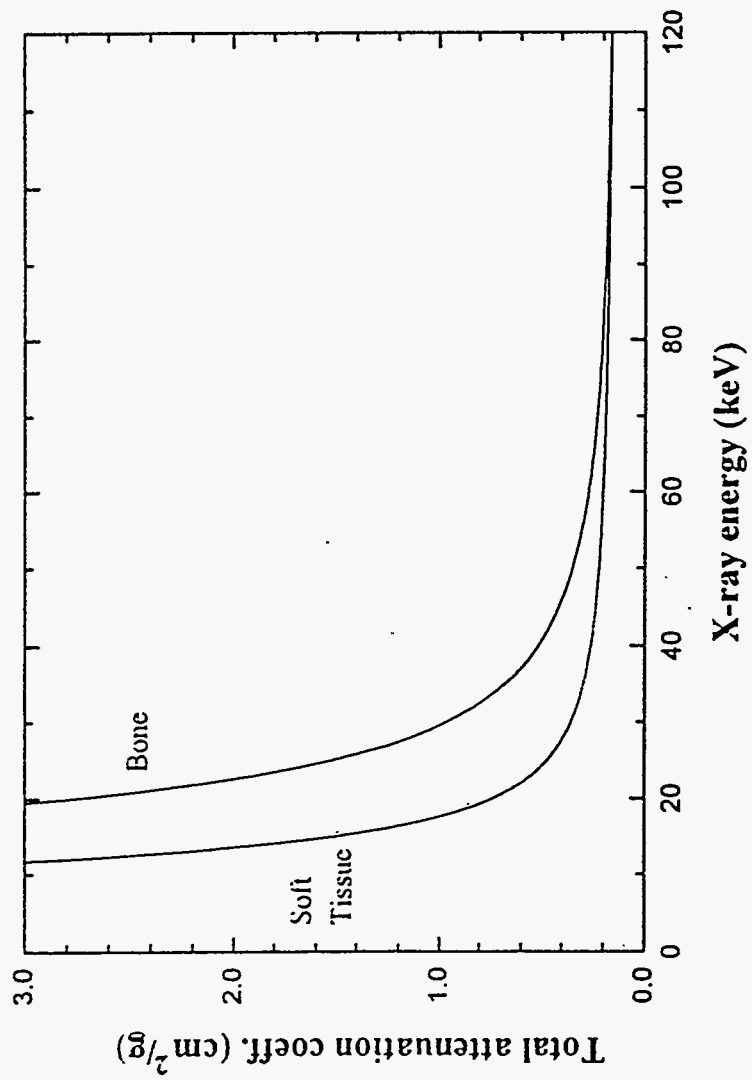


Figure 3

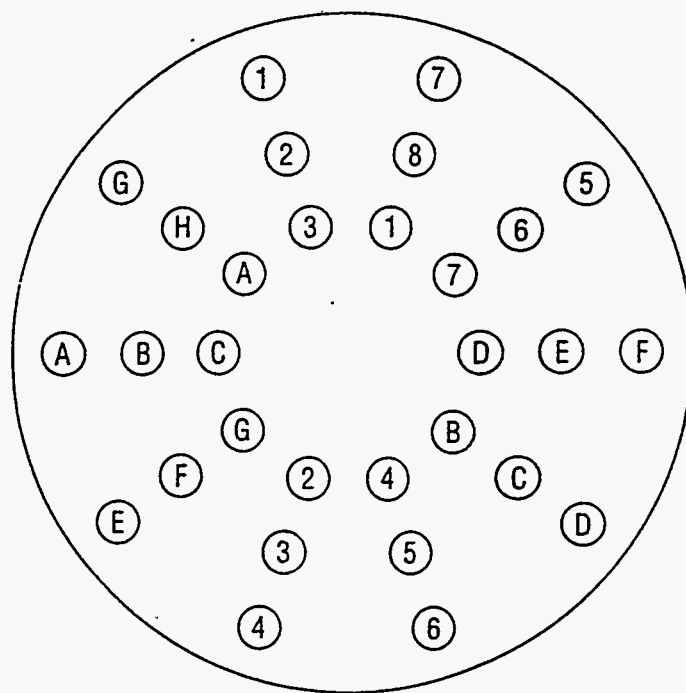


Figure 4

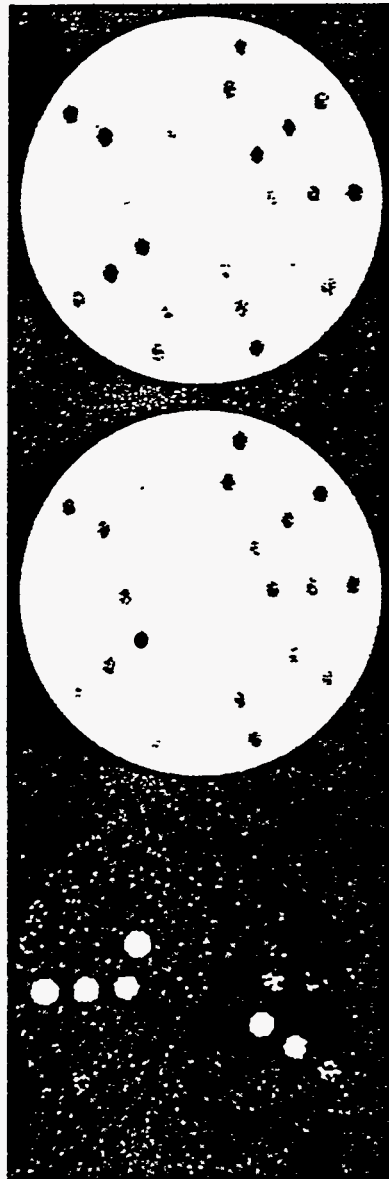


Figure. 5